Chapter 4

Instability and star formation in the Interstellar Medium

The correlation between atomic hydrogen density and star formation rate is a poorly understood problem in galaxies. A well defined power law relation with slope $\sim 1.0 \pm 0.2$ is observed between H_2 and SFR (Bigiel et al., 2008). However in the case of H I , though many nearby spiral galaxies show the relation between the H I density and SFR rate with indications that H I is being used up for star formation, establishing a definite relation like in the case of H_2 is still unsolved. Most of the studies consider the global average of the surface density of H I , H_2 and SFR for a given single galaxy and investigate the correlation for a galaxy sample. In such a study, uncertainties due to asymmetries and irregularities in the galactic disc are neglected. Moreover, H I is distributed in a much larger scale of the order of kpc, compared to the size of Gaint Molecular Clouds (GMC) and stars forming regions. The influence of H I dynamics on star formation activity can be scale-dependent. Hence rather than relying on azimuthally averaged global profiles, analysis using two dimensional intensity maps to be pursued for investigating the correlation between the H I distribution, dynamics and SFR. Similar studies in which two dimensional maps are being used to see the relationship between the disc instability and SFR have been

done in Elson et al. (2012); Marchuk and Sotnikova (2018); Yang et al. (2007). Marchuk and Sotnikova (2018) applied two fluid gravitational instability analysis on spiral galaxy NGC 628 and use Toomre criteria at each pixel of the two-dimensional image. Their results suggest that the azimuthal averaging process can make the disc more stable and hence probing star forming regions through instability analysis is not efficient. In this chapter, by implementing the gravitational disc instability model on individual galactic discs, we generate the two-dimensional map of the Toomre parameter to probe unstable regions in the various part of the disc.

Turbulence is found to play a significant role in the scenario of disc instability triggering star formation. There is observational evidence for the dual behaviour of turbulence where it both enhances and suppresses the star formation activity at the same time at different length scales (Mac Low and Klessen, 2004). Hence to understand the role of turbulence in disc instability and star formation, we also consider the presence of turbulence in our analysis.

4.1 Instability in two fluid disc

The dispersion relation for a gas disc of scale height h_z when it undergoes a perturbation which results in the axisymmetric waves of frequency ω is

$$\omega^2 = \kappa^2 - \frac{2\pi G\Sigma k}{1 + kh_z} + \sigma^2 k^2 \tag{4.1}$$

where wavenumber is k and κ is the epicyclic frequency. Σ is the surface density of the gas disc and σ is the sound speed (Romeo, 1994, 1992; Vandervoort, 1970). In case of instability, gravity term (second term of eq (4.1)) wins over the other two factors ; rotation and pressure and hence disc becomes unstable. Thus $\omega^2 < 0$ is the condition for instability. Hunter and Toomre (1969) proposed a condition for the instability in a thin disc of stars by

introducing Toomre parameter Q_* defined as,

$$Q_* = \frac{\kappa\sigma_*}{\pi G\Sigma_*}, \tag{4.2}$$

where σ_* is the stellar velocity dispersion and Σ_* is stellar surface density. Here whenever $Q_* < 1$, instability happens. The Toomre Criteria Q_g for gas components can also be defined as follows,

$$Q_g = \frac{\kappa\sigma_g}{\pi G\Sigma_g}, \tag{4.3}$$

where gas velocity dispersion is σ_g and gas surface density is Σ_g. Various instability studies on multicomponent systems (Bertin and Romeo, 1988; Elmegreen and Elmegreen, 1995; Jog, 1996; Rafikov, 2001; Romeo, 1994, 1992) show that interacting systems are more unstable than the systems where components are considered non-interacting. Rafikov (2001) gives a Toomre parameter (Q_T) for two fluid system of star and gas in a thin rotating disc as,

$$\frac{1}{Q_T} = \frac{2}{Q_*}\frac{q_*}{1+q_*^2} + \frac{2}{Q_g}\frac{q_g}{1+q_g^2}, \tag{4.4}$$

here Q_g and Q_* are the respective single fluid Toomre parameters, $q_* = \frac{k\sigma_*}{\kappa}$ and $q_g = \frac{k\sigma_g}{\kappa}$. Single component Toomre parameters Q_g and Q_* are defined as in eq (4.3) and eq (4.2) respectively. In this analysis, we consider the two fluid disc model, where star and gas are the two interacting fluids in the disc and use Toomre parameter Q_T in eq (4.4) for instability criteria. The following discusses how we can estimate different terms in eq (4.4) in detail.

Epicyclic frequency κ was calculated from the rotation curve by the following conventional definition (see Binney and Tremaine (2008)),

$$\kappa^2 = \frac{2V(R)}{R}\left(\frac{dV(R)}{dR} + \frac{V(R)}{R}\right). \tag{4.5}$$

Here $V(R)$ is the tangential rotation of the galactic disc as a function of galactic radius R. We estimate the stellar surface Σ_* by dividing the Stellar mass maps from observations by the pixel area A. By assuming hydrostatic equilibrium, van der Kruit (1988) shows that stellar velocity dispersion σ_* is related to Σ_* as follows,

$$\sigma_* = \sqrt{2\pi G \Sigma_* h_*},$$

where h_* is the scale height of stellar disc. We use the same relation in our analysis for the estimation of the stellar velocity dispersion.

The gas component in our model mainly comprises of two; atomic hydrogen H I and molecular hydrogen $\mathrm{H_2}$. Burkhart and Lazarian (2012) show that in presence of turbulence the density fluctuations modifies through the Mach number of the turbulence. Incorporating this effect we write the gas surface density as

$$\Sigma_g(k) = \frac{\left(\Sigma_{\mathrm{HI}}(k)\sqrt{1+\frac{1}{4}M^2} + \Sigma_{\mathrm{H_2}}(k)\sqrt{1+\frac{2.38}{4}M^2}\right)\cos(i) \times 1.36}{1+kh_z}. \tag{4.6}$$

Here the Σ_{HI} and $\Sigma_{\mathrm{H_2}}$ are the individual surface density of H I and molecular hydrogen. M is the Mach number and h_z is the local scale height of the gas. The inclination effect in the column density measurement is taken care of by including the cosine of inclination angle i and to take into account the mass fraction of Helium in the ISM, we multiplied the entire Σ_g by 1.36. Using the conventional definition of Mach number, we found that the Mach number of $\mathrm{H_2}$ is $\sqrt{2.38}$ times that of H I due to the difference in mass and degree of freedom. We use this conversion factor in above expression. Note that we here assume that scale height of gas disc and stellar disc as same in the entire analysis.

Numerous simulations and analytic results shows that the density distribution of supersonic isothermal turbulent ISM show log-normal distribution (Burkhart et al., 2010; Klessen, 2000; Kritsuk et al., 2007; Mocz and Burkhart, 2019; Molina et al., 2012; Padoan

and Nordlund, 2011; Passot and Vázquez-Semadeni, 1998; Price et al., 2011). The variance of such a distribution increases with the Mach number M in the medium. However, due to the presence of strong shocks and correlated density structures, column density probability density functions (PDF) show deviations from the lognormal distribution in many recent simulations (Bialy et al., 2017; Federrath et al., 2010, 2009; Kritsuk et al., 2007; Schmidt et al., 2009) and several observations (Sharda et al., 2022). Robertson and Goldreich (2018) theoretically suggest that the shocks in the turbulent medium produce a high mass fraction in the density distribution which is reflected as an elongated tail at the higher end of the PDF. Another analytical model put forward to describe this intermittency of density PDF was by Squire and Hopkins (2017), where they considered the density as a collection of strong shocks having width M^{-1}. Hopkins (2013) introduced a new fitting function for the density probability function in turbulent, ideal gas considering this non-lognormality behaviour. He modelled the volume weighted density function as Eq 5 in Hopkins (2013). We use this two-parameter function to model the H I density PDF and the fitting parameters are directly related to the Mach Number M and peak column density $N_{\rm HI}$.

4.2 Sample selection and observations

We choose a set of three galaxies, namely NGC 5236, NGC 4736 and NGC 3351 for this analysis. Details of these galaxies are given in table 4.1. These galaxies in our sample are significantly different in their morphology. Though all of them are barred spiral galaxies, spiral distribution is different in all of them. For instance, NGC 5236 is a grand design spiral galaxy where spiral arms are prominently visible with an elongated bar. In NGC 4736 spiral arms are distinguishable and have a weak nuclear bar. The galaxy has a bright ring of star formation prominently visible in Hff emission which of radius $\sim$ 1 kpc (Wong and Blitz, 2000). Another fainter ring is also located about 6 kpc from the galactic centre (Sandage, 1961). We can barely distinguish the spirals in NGC 3351, more looks

Galaxy	Type	Dist (Mpc)	PA (deg)	i (deg)	R_{25} (kpc)	$R_{\rm HI}$ (kpc)	$\log \mathrm{M_{HI}}$ $\mathrm{M_\odot}$	$\log \mathrm{M_*}$ $\mathrm{M_\odot}$	$\log \mathrm{M_{H_2}}$ $\mathrm{M_\odot}$	SFR $\mathrm{M_\odot yr^{-1}}$
NGC 5236	SABc	4.84	225	24	10.9	21.12	9.27	10.53	8.99	2.52
NGC 4736	SABa	5.00	296	41	5.64	13.09	8.63	10.46	8.12	0.43
NGC 3351	SBb	10.00	192	21	10.53	18.00	9.07	10.44	8.60	0.71

Table 4.1 Following details of the three galaxies are given here; Morphology type, Distance, position angle, inclination, optical size(R_{25}), $R_{\rm HI}$ radius corresponding to semi major axis extent at a H I column density of 10^{19} atoms cm^{-2}, total H I mass from integrating values within the H I extent, total stellar mass and total molecular mass from integrating values within in $1.5R_{25}$ and star formation rate. References as follows: (1) Walter et al. (2008), (2) de Blok et al. (2008), (3) Bottinelli and Gouguenheim (1973), (4) Leroy et al. (2008), (5) Ann et al. (2015) and (6) Crowther (2013)

like a flocculent spiral galaxy in H I maps. It is a starburst galaxy and it has ring structure (Colina et al., 1997; Elmegreen et al., 1997). Star formation regions are located in nuclear ring around the galaxy with major axis ~ 630 pc (Colina et al., 2009). Walter et al. (2008) provide the H I global spectral profile of these three galaxies;- NGC 5236 and NGC 4736 have asymmetrical double horn features while NGC 3351 has a nice symmetrical double horn profile. The H I column density power spectrum measurement of these galaxies shows power law behaviour (Dutta et al., 2008; Nandakumar and Dutta, 2020) and slope of power law of NGC 5236, NGC 4736 and NGC 3351 are $-1.23, 0.7, 0.33$ respectively.

We use the following archival observations for different components in the two-fluid model.

- **H I intensity and velocity dispersion map :** We use the publicly available H I moment maps of these three galaxies from the THINGS survey (Walter et al., 2008). The H I moment zero maps are converted to H I surface density map as follows:

$$\frac{\Sigma_{\rm HI}}{[\mathrm{kg\ m^{-2}}]} = 1.823 \times 10^{18} \times 6.07 \times 10^{6} \frac{m_{\rm HI}(\mathrm{kg})}{\mathrm{B_{maj}}(") \times \mathrm{B_{min}}(")} \times \frac{M_0}{[\mathrm{Jy/beam\ m/s}]} \quad (4.7)$$

- **Molecular hydrogen maps:** Nobeyama survey provides CO (J $= 1-0$) maps of 40 nearby spiral galaxies observed by Nobeyama 45 m single dish telescope and the BIMA Survey of Nearby Galaxies is imaging CO(J $= 1-0$) emissions of 44 nearby spiral galaxies (Helfer et al., 2003; Kuno et al., 2007). We use the archival observation of CO (J$= 1-0$) data from Nobeyama survey and BIMA survey for the three galaxies. The typical spatial resolution of the BIMA survey is 6" which is better than single dish observations by Nobeyama. Though NGC 4736 and NGC 3351 are observed in both surveys, NGC 3351 BIMA survey maps are sparsed, hence we use Nobeyama data for NGC 3351. NGC 5236 was available from Nobeyama survey and we used it. $\Sigma_{\mathrm{H_2}}$ is the surface mass density of molecular hydrogen converted from the integrated CO maps I_{CO}(Kuno et al., 2007; Leroy et al., 2008; Walter et al., 2008) as follows,

$$\frac{\Sigma_{\mathrm{H_2}}}{[\mathrm{kg\ m^{-2}}]} = \frac{X_{CO}}{[(\mathrm{K\ km\ s^{-1}})^{-1}\ \mathrm{m^{-2}}]} \times \frac{m_{\mathrm{H_2}}}{[\mathrm{kg}]} \times \frac{I_{CO}}{[\mathrm{K\ km\ s^{-1}}]} \tag{4.8}$$

where X_{CO} is the CO-to-H_2 conversion factor which is taken as $0.9\times10^{24}\ (\mathrm{K\ km\ s^{-1}})^{-1}$.

- **Stellar mass and star formation rate map :** We rely on mid-IR emission for probing stellar mass distribution and star formation histories in these galaxies. The Wide-field Infrared Survey Explorer (WISE) is a highly sensitive all sky mid-infrared survey that observed at four mid infrared bands centered at $3.4\ \mu m$, $4.6\ \mu m$, $12\ \mu m$ and $22\ \mu m$ using 40 cm space infrared telescope (Wright et al., 2010). The first two bands trace the stellar components in the galaxies hence star mass distribution can be generated using these two bands (Jarrett et al., 2013). W3 band traces PAH (polycyclic aromatic hydrocarbon) which are essentially excited by ultraviolet radiation from both young, and old, evolved stars. Hence it is the most efficient

Galaxy	Star WISE resolution (pc)	H_2 CO(J=1−0) Grid Size/B_{maj} (pc)	H I THINGS $B_{maj} \times B_{min}$ (pc)	H I THINGS Δv (km sec^{-1})	references
NGC 5236	281	258	244×131	2.6	1,2,3
NGC 4736	291	140	144×134	5.2	1,2,4
NGC 3351	582	500	303×251	5.2	1,2,3

Table 4.2 Table giving observation details of the three galaxies. H I maps are from THINGS, H_2 maps are derived from CO maps of the Nobeyama survey and the BIMA survey. The star mass maps are obtained from WISE survey and both have the same resolution parameters. References as follow (1) Walter et al. (2008), (2) Jarrett et al. (2013), (3) Kuno et al. (2007), (4) Helfer et al. (2003).

SFR tracer in the WISE survey. The fourth band at 22 μm is sensitive toward the emission from warm dust which mostly traces recent massive star-forming regions Jarrett et al. (2013). We use the processed star mass maps and SFR maps from this survey for all three galaxies in this analysis (Jarrett et al., 2019)[1]. The star mass maps are generated using $3.4\ \mu m$ and $4.6\ \mu m$ band and SFR maps are generated using $12\ \mu m$ band. The detailed analysis and calibration procedure for the generation of these maps are given in Cluver et al. (2017); Jarrett et al. (2013, 2019). The typical resolutions of WISE images range from $\sim 6"-8"$ for lower bands and 12" for higher bands (Jarrett et al., 2012). Hence final star mass maps are smoothed to the resolution of SFR maps (12") which are obtained from high band at $12\ \mu m$.

The surface density maps of stellar mass are calculated as follows,

$$\Sigma_* = \frac{M_*}{\Delta x \Delta y} \cos(i), \tag{4.9}$$

[1]We are indebted to Prof. Tom Jarret for the data.

where Δx and Δy are the grid space of the mass maps. We include the cosine of inclination angle like in Σ_g to correct for the inclination effect.

- **Rotation curve :** We estimate the rotation curve for NGC 5236 and NGC 3351 from the line of sight velocity map (M_1) using a tilted ring model fitting with the software BBarolo (Di Teodoro and Fraternali, 2015). We use the rotation curve estimated by de Blok et al. (2008) for NGC 4736. Thus κ are estimated using eq (4.5).

Table 4.2 contains details about image resolution and spectral resolution for different data for three galaxies.

4.3 Estimation of two-fluid Toomre parameter

In the estimation of two-fluid Toomre parameter Q_T at each pixel in the two-dimensional map, the first is the generation of the fitting parameters of non-lognormal function as discussed in section 4.1. We use the H I intensity moment maps properly converted to column density units, for this exercise. Around each pixel in the input map, a square box was chosen with radius $\lambda = \frac{2\pi}{k}$ and the probability density function (PDF) of all pixels is estimated. The PDF is modelled according to the non-lognormal function discussed in Hopkins (2013) and the best fit parameters are found using chi-square estimation. The peak value of the column density distribution and Mach number M are the two parameters of the model. We repeat this exercise for all pixels and hence maps of these two parameters are found. Similarly in the H I velocity dispersion map, for each pixel, we choose a box around it with the same size and calculate the median of all pixel values inside the box. Hence we estimate the median of H I velocity dispersion ($\sigma_{\rm HI}$) at each pixel which is used as gas velocity dispersion σ_g as in eq (4.4).

The surface density maps of stellar mass, molecular hydrogen and SFR are directly used from the observational data after proper conversion as mentioned in section 4.2. Note

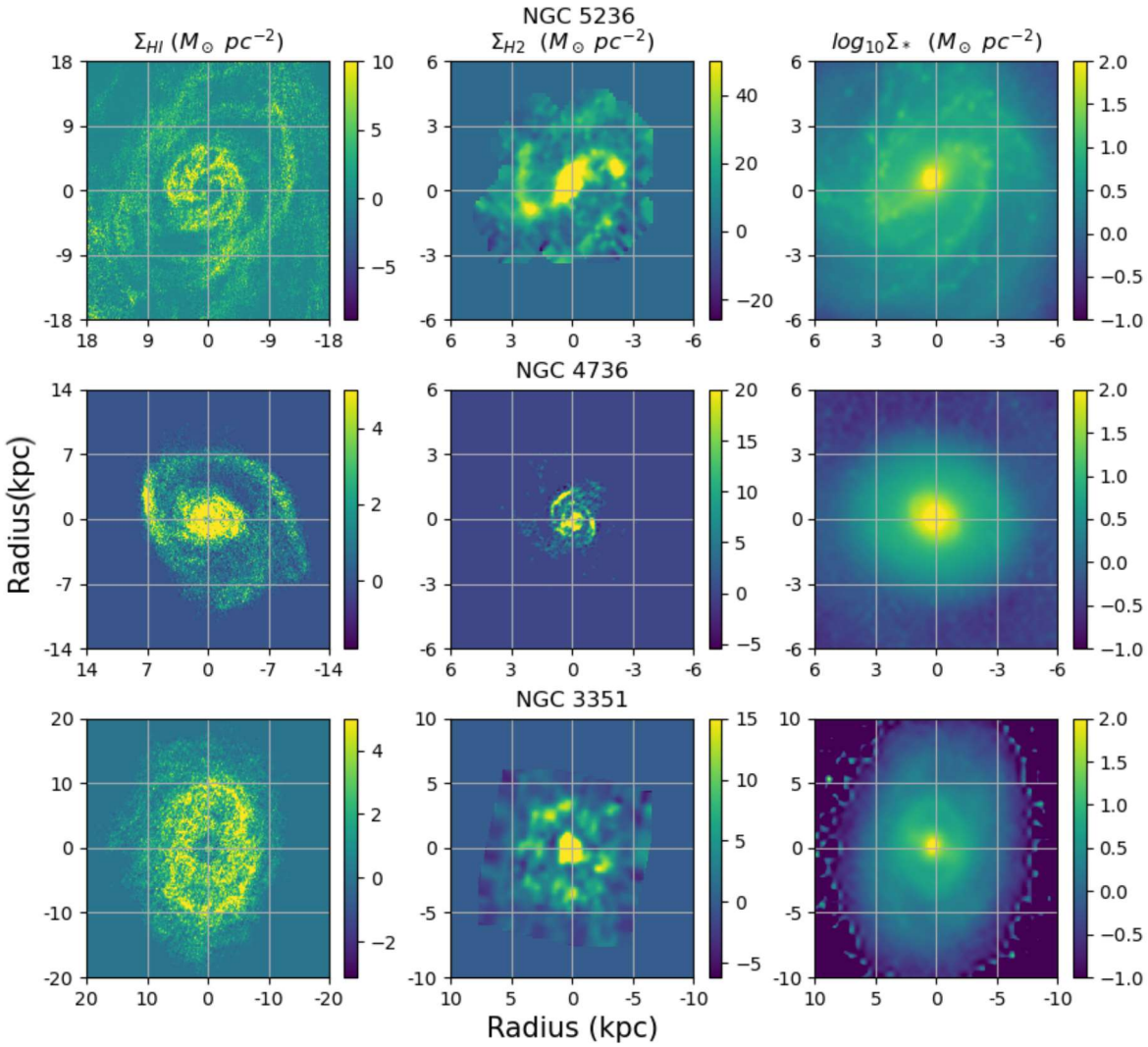

Fig. 4.1 Left column shows the H I surface density maps of three galaxies after grid matching. The Middle column is H_2 surface density and the right column is star mass density maps.

that, the resolution and grid size of different observation data are different. We smoothed all these maps to a common (lowest) resolution (with grid space ~ 6") and re-grid the maps. The final maps have a pixel size corresponding to the length scale of 140 pc, 145 pc and 290 pc for NGC 5236, NGC 4736 and NGC 3351 respectively. We obtained the surface density maps of H I , H_2 and stellar mass of three galaxies after grid matching as shown in fig 4.1.

We choose the value of scale height h_z as follows. Kregel et al. (2004) study the H I content of several edge-on galaxies and found that the ratio of H I disc thickness to the H I scale length $\sim 0.06 \pm 0.015$ at $1 M_{\odot} pc^{-2}$. Using this relation the approximate values of scale height for NGC 5236, NGC 4736, NGC 3351 are $1.2, 0.74, 1.1$ kpc. Dutta (2009) showed that the density power spectrum steepens at the length scales corresponding to the scale height of the disc, indicating a transition from 2D turbulence to 3D turbulence (Dutta et al., 2009). Nandakumar and Dutta (2020) have measured H I density and velocity power spectrum of NGC 5236 over a large length scale of two decades. They couldn't see any such steepening in their power spectrum until 300 pc and hence conclude that the scale height of the NGC 5236 galaxy is less than 300 pc. This scale height value is nearly one fourth of the values calculated using relation in Kregel et al. (2004). Assuming that the other two galaxies follow this similar trend we choose the values of scale height to be $h_z = 290, 180, 270$ pc for NGC 5236, NGC 4736 and NGC 3351 respectively.

To investigate the trend of disc instability with respect to length scale and further to see how H I turbulence is correlated with star formation at different scales, we repeat the above procedure to generate the Q_T maps for different values of λ. The Q_T maps are generated for the following scales starting from the resolution limit of the maps to the scales comparable to the galactic size, $\lambda = 350$ pc, 500 pc, 800 pc, 1 kpc, 1.1 kpc, 1.5 kpc , 2 kpc , 3 kpc and 4 kpc. Hence we are able to see the scale dependence of the Q_T distribution in the galactic disc.

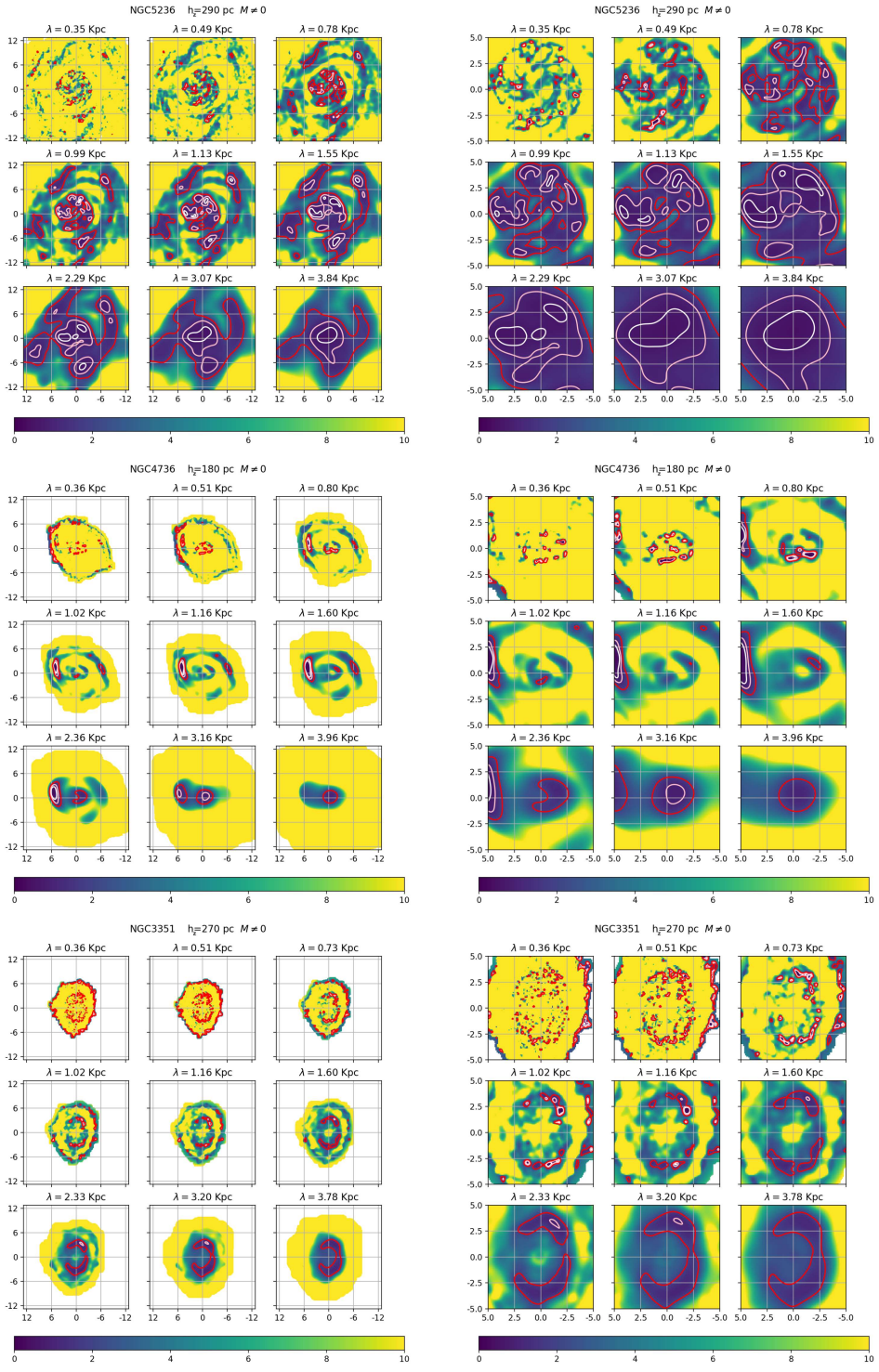

Fig. 4.2 Each row in the Left column shows the two fluid Toomre parameter Q_T estimated in entire region in three galaxies for different wavelength scales. Each row in the right column shows galactic center only in enlarged view for the respective plots.

4.4 Results and Inferences

Figure 4.2 shows the density plot of Q_T for different k or $\lambda = 2\pi/k$ for the three galaxies. The left column shows the entire galactic region and right column shows the enlarged view of the stellar disc. Red contours represent $Q_T = 2.5$, pink contours mark $Q_T = 1$ and white contours are $Q_T = 0.6$. Leroy et al. (2008)'s work on the two fluid gravitational stability analysis on 23 nearby galaxies shows that most of the $Q_{star+gas}$ values lies between $1.3 - 2.5$. Elmegreen (2011) considers the effect of turbulent dissipation in the dispersion relation of instability and shows that instability criteria for Q_T value should be around 2-3. Similar conclusions are drawn with observational data of several spiral galaxies by Marchuk and Sotnikova (2018), that instability criteria should be $Q_T < 0.5 - 2.5$. Considering these we identify the contour regions in Fig 4.2 as either unstable or marginally unstable after assuming $Q_T \sim 2$ as the boundary of instability.

For NGC 5236, we see that at smaller $\lambda < 500$pc, the unstable regions are fragmented and are within the stellar disc. As we increase λ these regions merge and start to trace the spiral arms. For large enough λ (> 2 kpc), a single contour over the stellar disc denotes the region of instability. This indicates a correlation between instability and star formation, as towards the centre star formation is always high. Moreover, introduction of the stellar component in stability analysis always increases instability, as the star mass enhances the gravity term (Leroy et al., 2008). Hence the highest distribution of star mass in the central region of the disc can also lead the disc to instability. For NGC 4736 we still see small fragmented regions of instability for smaller values of λ, however at intermediate scales (~ 1 kpc) one of the spiral arms and central part of the galaxy show hint of instability, which further reduces at a larger scale. NGC 3351 shows pockets of instability to the intermediate scales (~ 1 kpc) and when averaged to larger scales, unstable regions disappear.

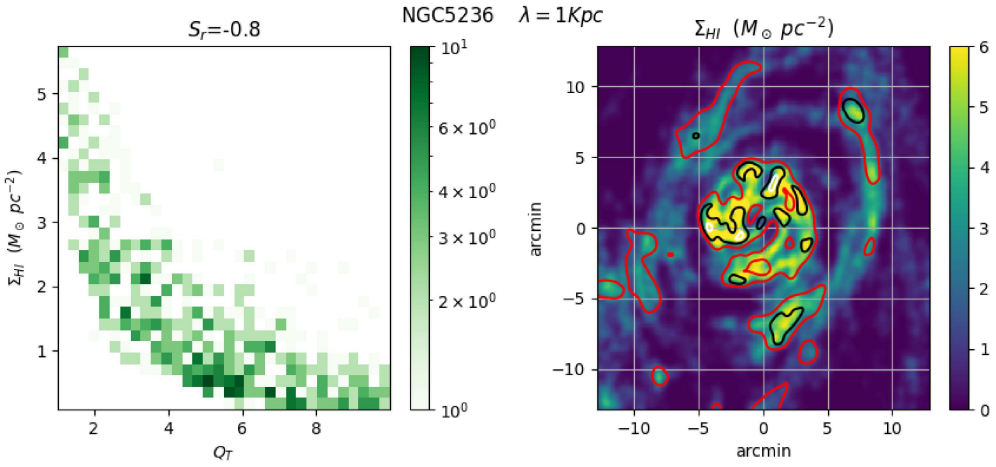

Fig. 4.3 Left panel of figure 4.3 shows the distribution of pixels in $Q_T - \Sigma_{\rm HI}$ plane in a density plot giving the number of pixels in a given range. Right hand side of figure 4.3 shows the $\Sigma_{\rm HI}$ with overplot of Q_T values equals to 2,1,0.6 as red, black, white contours respectively. The values are noted at the top of the panel.

The identification of resolved giant molecular clouds in galaxies NGC 5236 and NGC 4736 shows that majority of them are populated inside the R_{25} and located along the spiral arms (Donovan Meyer et al., 2013; Heiner et al., 2008). Wong and Blitz (2000) estimated the azimuthally averaged radial variation Q parameter for gas only disc, where the minimum of Q was found in the location of the high SF ring. The unstable regions that are seen in Q_T maps of NGC 4736 are also found to be around these two rings, which indicates high SF regions are correlated with instability. In all three galaxies, most of the unstable regions seen at finer resolutions happened to lie among the spiral arms, the active location of star formation.

4.4.1 Correlation with H I

Our analysis discussed above gives a clear indication that probed unstable regions are strongly related to high star forming regions in the disc. Similarly, it is also important to see the distribution of H I density in these unstable regions. For instance, a simple visual representation to see any relation is overplotting one quantity on top of the other as in the

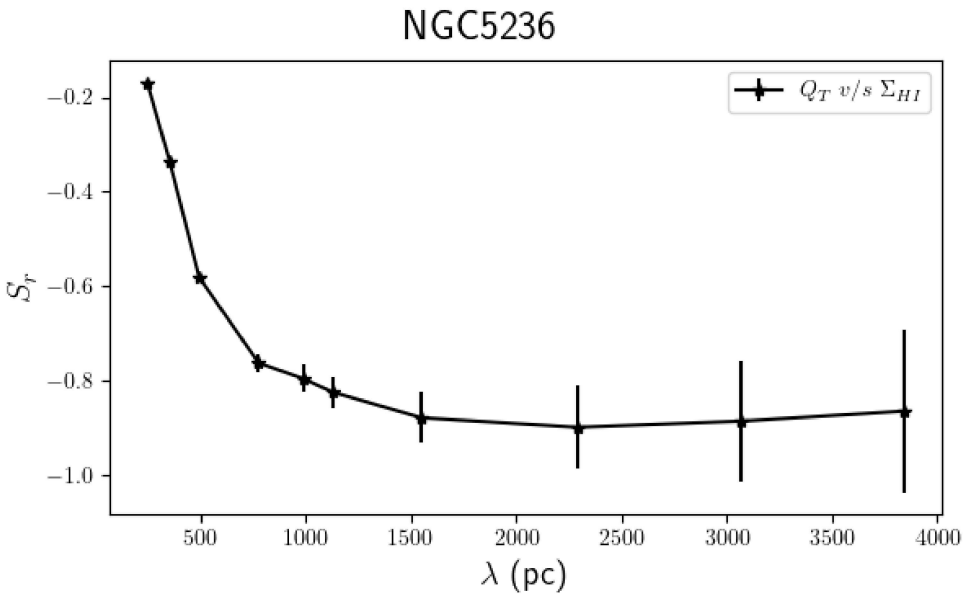

(a)

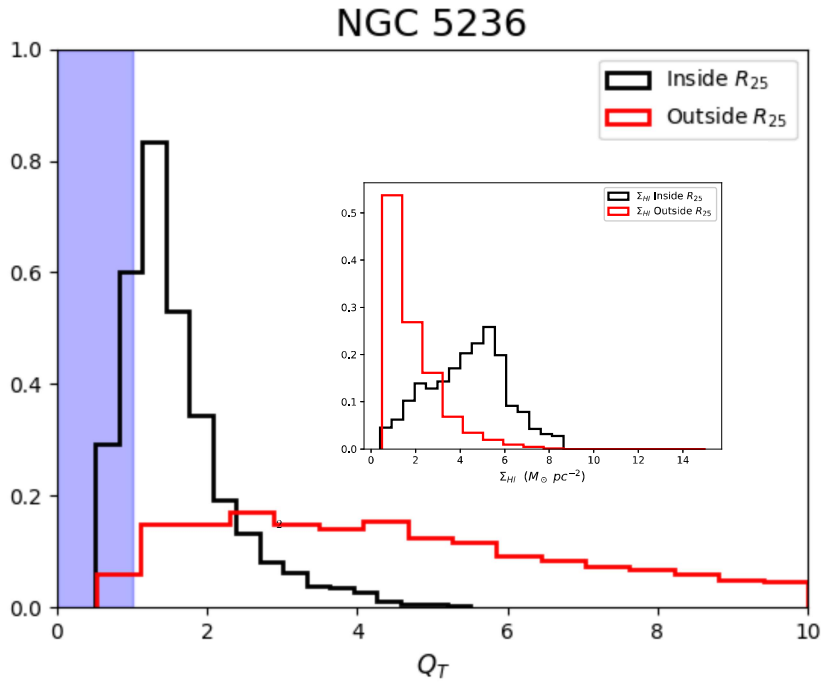

(b)

Fig. 4.4 Figure (a) is the Spearman correlation coefficient of Q_T and $\Sigma_{\rm HI}$ are plotted as function of λ in parsec for NGC 5236. Figure (b) shows the separate probability density of Q_T values at $\lambda \sim 1$ kpc inside (black) and outside (red) the stellar disc. Blue shaded region shows the $Q_T < 1$ region. Histogram plot show in the inset is that of $\Sigma_{\rm HI}$ with legend follows the same order.

right hand side of figure 4.3. It shows the $\Sigma_{\rm HI}$ for $\lambda = 1$ kpc in a density plot with Q_T values equal to 2,1,0.6 shown with red, black, and white contours respectively. Colorbar represent the values of $\Sigma_{\rm HI}$. It is clear from the plot, that many of the detected unstable regions are overlapping with high density region of H I in the galaxy. To quantify this relation, we estimate the Spearman correlation coefficient of the two quantity as follows. We identify values of $\Sigma_{\rm HI}$ and Q_T at the same pixel and plot them against each other in a density plot. We consider the pixels with values of $0 < Q_T < 10$ and H I density greater than a threshold to avoid noise effects. The left panel of figure 4.3 shows the distribution of pixels in $Q_T - \Sigma_{\rm HI}$ plane in a density plot giving the number of pixels in a given range for the entire galaxy. Colobar shows the frequency of the values in each bin. The density plot show a strong anti-correlation with Spearman correlation factor of $S_r = -0.8$ for this particular length scale $\lambda = 1$ kpc.

To capture the scale dependence of this correlation between H I density and instability, we estimate the Spearman correlation coefficient at different λ in a similar way. Figure 4.4(a) shows the correlation coefficient S_r between Q_T and $\Sigma_{\rm HI}$ as a function of different scales. Error bars represent the sample variance of the respective values. It is visible that H I column density is strongly anti-correlated with Q_T for $\lambda > 1$ kpc. This means large scale high density H I regions (> 1 kpc) in the galactic disc are prone to instability. The spiral arms are the active regions of star formation, where the majority of the GMCs are located (Donovan Meyer et al., 2013), their typical size starts from 1 kpc. Moreover, the unstable regions in the NGC 5236 galaxy are also following the spiral structures in the disc (see figure 4.2). Hence this is a piece of clear evidence that, H I density at a large scale is indirectly fueling star formation by triggering instability. However, at a smaller scale < 500pc, H I density seems not correlated with the Q_T values. In small scales, H I is being already used up for the star formation by transferring to GMC and hence role of H I at the scale becomes insignificant. Figure 4.4(b) show the distribution of Q_T values from

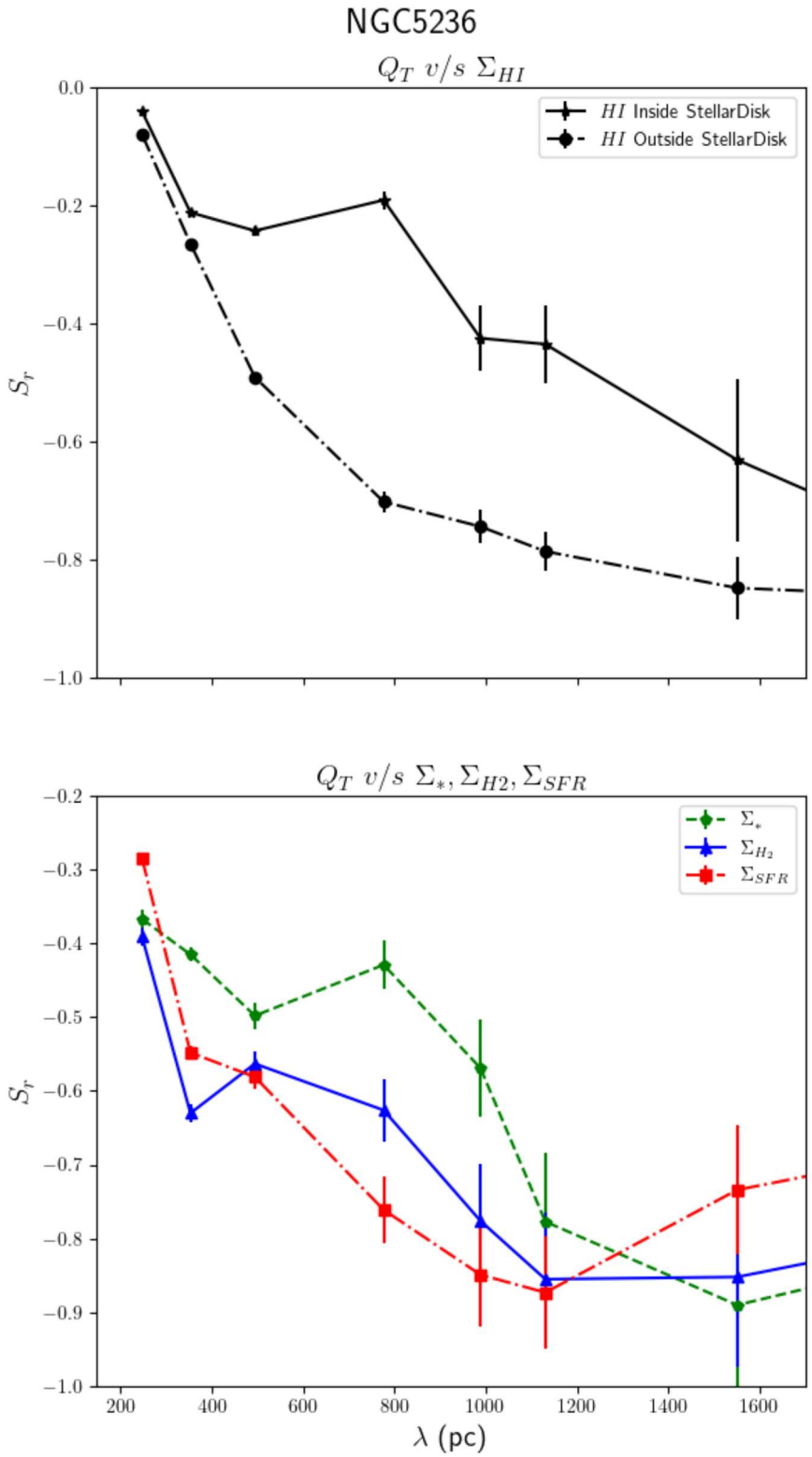

Fig. 4.5 The correlation coefficient between Q_T and different surface densities are plotted as a function of λ in parsec for all three galaxies. First row shows the correlation between Q_T and H I from inside and outside the stellar disc. Second row shows that between Q_T and surface density of H_2, stellar mass and SFR in blue, green and red lines respectively.

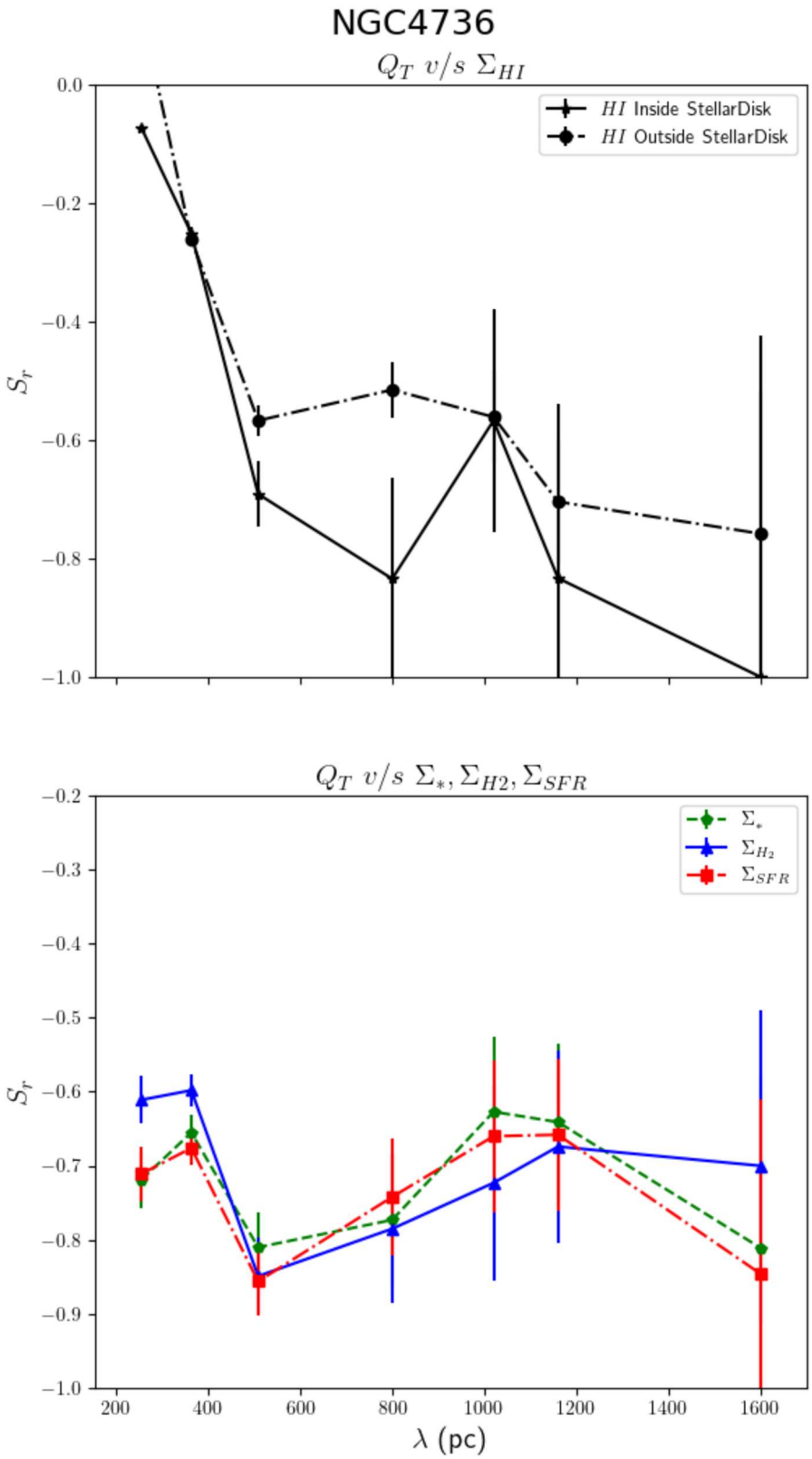

Fig. 4.5 continued for NGC 4736

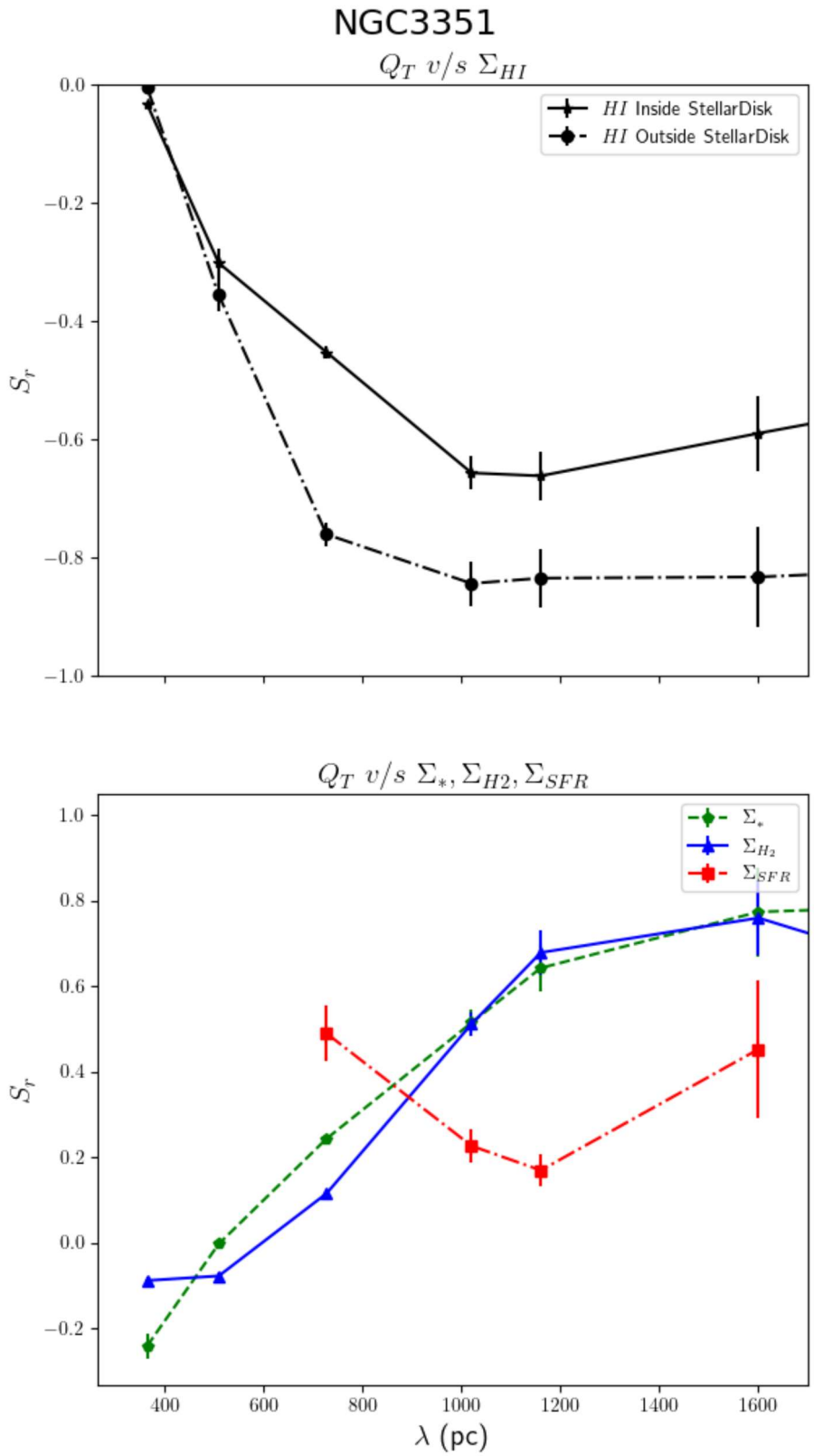

Fig. 4.5 continued for NGC 3351

inside and outside the stellar disc separately, with the blue shade indicating the region with $Q_T < 1$. The H I gas within the stellar region seems to be more unstable, whereas the gas outside is mostly stable. Inside the stellar disc, contribution from the stellar mass enhances the gravity term giving rise to instability.

4.4.2 Correlation with H_2, Σ_*, SFR

We repeat the exercise to see the correlation with other components in the disc. We estimate the Spearman correlation coeffcient as previously discussed for Q_T and the following quantities at different length scales ; H_2 density, stellar mass and star formation rate. Figure 4.5 shows the correlation between Q_T and surface density of atomic and molecular hydrogen, stellar mass and star formation rate for all three galaxies for $\lambda < 1.6$ kpc. The top panel show Spearman correlation of Q_T with atomic hydrogen that presents inside and outside the stellar disc separately. The bottom panel shows the S_r values between Q_T and surface density of H_2 (blue line), star(green line) and SFR(red line) are given as a function of length scales. All surface densities follow an anti-correlation trend with Q_T at larger scales > 1 kpc in NGC 5236 and NGC 4736. This can be interpreted as follows; at larger scales, high gas density regions (both H I and H_2) in the disc are prone to instability and can result in gas clouds collapsing. The positive correlation of unstable regions with a high star formation rate tells that, the chance of thus formed collapsed cloud to form stars are also high. On the other hand, at smaller scales, molecular hydrogen, stellar mass and star formation rate are showing a similar trend of uncorrelation like in the case of H I . In NGC 4736, correlation values are in the intermediate range giving a hint of anti-correlation at smaller scales < 500 pc. H I density is expected to be not correlated with instability at smaller scales, as much gas gets used up already for GMC's formation at these scales. However, the molecular hydrogen and SFR are expected to follow a trend with Q_T which we do not see here. Note that the smaller scales that we probe here are limited

to roughly 2-3 times of resolution element, hence we cannot also ignore the possibility of uncertainties due to resolution limit. Unlike the other two galaxies, for NGC 3351 three surface densities $\Sigma_{*/\mathrm{H_2/SFR}}$ are strongly correlated with high Q_T values at larger scales > 1 kpc and uncorrelated at smaller scales. The H I surface density remains to show a correlation trend with instability like in the other two galaxies at similar scales. Among the these three galaxies, NGC 5236 has significantly large star formation rate per unit area ($\sim 0.07\ \mathrm{M_\odot\ yr^{-1}\ kpc^{-2}}$), while NGC 3351 has the least ($\sim 0.009\ \mathrm{M_\odot\ yr^{-1}\ kpc^{-2}}$). The NGC 4736 has $\sim 0.042\ \mathrm{M_\odot\ yr^{-1}\ kpc^{-2}}$ star formation rate per unit area. The large scale behaviour of instability as seen above also follows this trend.

In this scenario, possibly the disc instability is failing to form new stars. Though higher H I density regions can undergo gravitational instability, resultant collapse may not meet the criteria that lead to the formation of smaller structures. Note that, unlike in the galaxies NGC 4736 and NGC 5236, for the galaxy NGC 3351 high molecular hydrogen regions are more likely to be stable, which also effectively delays star formation. Naturally, a question arises. Is there any other process or dynamics involved here? The following subsection tries to answer this issue.

4.4.3 Role of turbulence

It is always not necessary that cloud collapse triggered by gravitational instability can lead to star formation unless it goes below the Jeans length scales. But hence formed cloud collapses can eventually induce turbulence which makes the gas fragmented and they further collapse to smaller scales. The generated turbulence cascade down to a smaller scale which helps the cloud to collapse to the scale of Jeans length and this way it helps the collapsing process to form structures (Elmegreen, 2002). On other hand, if the dispersion in turbulent gas is too high, it results in the quenching of star formation. Many observational evidences are available in literature which show, how turbulences trigger star formation

in disc galaxies (Elmegreen and Hunter, 2006; Kraljic et al., 2014) as well as quench star formation (Murray et al., 2010; Ostriker and Shetty, 2011). In our analysis, the contribution of turbulence is not only due to the addition of Mach number M in the gravity term but also included in velocity dispersion of H I . Tamburro et al. (2009) have shown through the estimation of H I line width in 11 spiral galaxies (where NGC 4736 and NGC 3351 are included) that, H I line width is found to be much wider than the expected thermal value ($\sim$8 km sec^{-1}), especially inside the stellar disc ($< R_{25}$). They have shown that high velocity width observed in their sample is possibly due to turbulence. Similarly from the measurement of the turbulent velocity fluctuations in NGC 5236 and NGC 6946 (see Chapter 3), we show that the total velocity dispersion has a significant contribution from turbulence driving too. Instead of assuming a constant value of H I gas dispersion which is widely adopted in much literature on stability analysis (Boissier et al. (2003); Leroy et al. (2008); Martin and Kennicutt (2001); Wong and Blitz (2000) etc), here we used the observationally derived H I velocity dispersion maps. Hence the effect of high H I gas velocity dispersion regions originally driven by turbulence at the different parts of the disc can be included in our investigation. Hence this analysis takes into account both dual behaviour of the turbulence in the star formation activity.

We do a similar analysis to assess the effect of gas dispersion by estimating the Spearman correlation coefficient between gas dispersion $\sigma_{\rm HI}$ and different quantities like Q_T, $\Sigma_{*/SFR/gas}$ at different λ. Figure 4.6 shows the Spearman correlation coefficient between $\sigma_{\rm HI}$ and Q_T, Σ_{SFR}, $\Sigma_{\rm HI}$, $\Sigma_{\rm H_2}$ and Σ_* plotted as function of λ in parsec for three galaxies. In the left panel, the red line with star points shows the correlation coefficient between $\sigma_{\rm HI}$ and $\Sigma_{\rm HI}$, the black line with square markers shows that of $\sigma_{\rm HI}$ and Σ_{SFR} and the blue line with triangle markers shows the same for $\sigma_{\rm HI}$ and Q_T. We show the correlation between $\sigma_{\rm HI}$ and $\Sigma_{\rm H_2}$, Σ_* in the right panel with green lines with square points and purple lines with circles respectively. The first row shows the plots for NGC 5236, the second

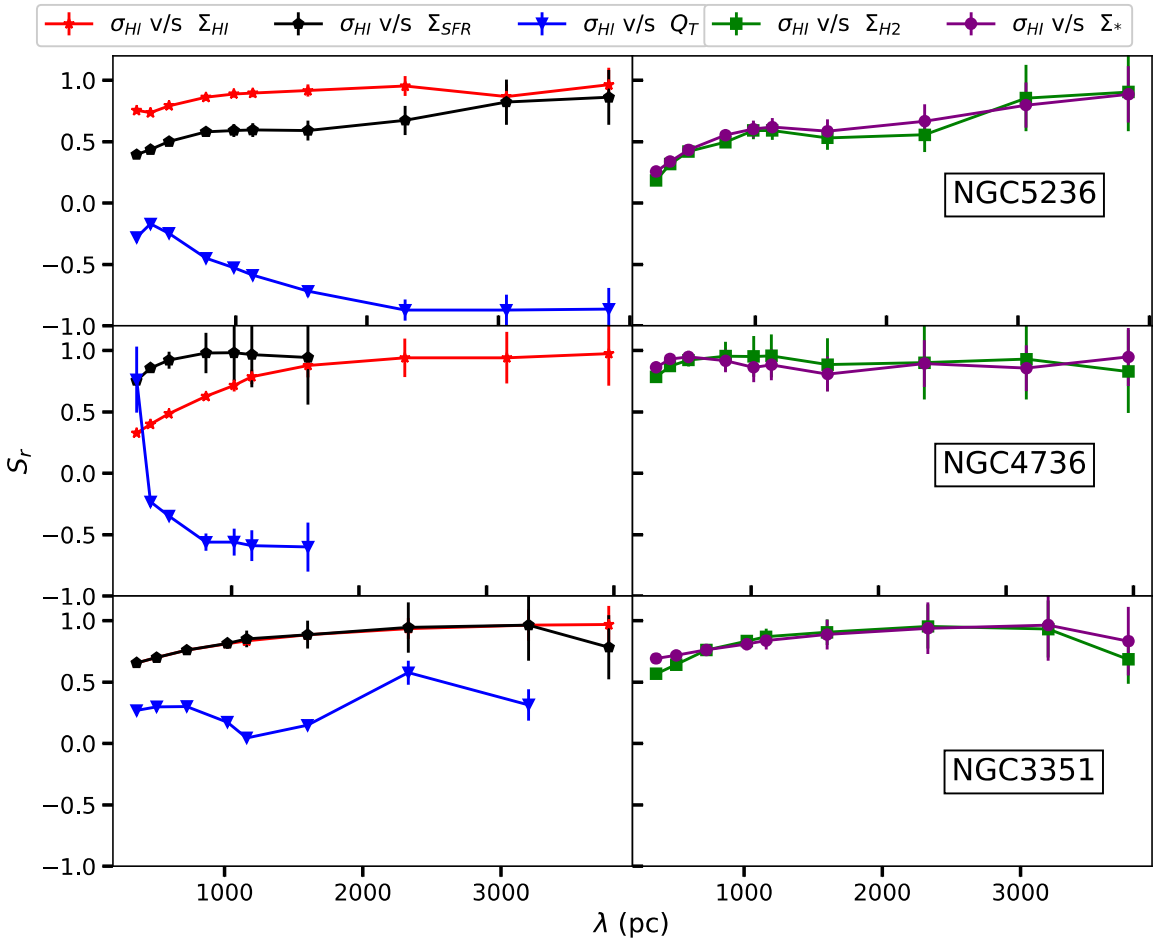

Fig. 4.6 The spearman correlation coefficient between $\sigma_{\rm HI}$ and Q_T, Σ_{SFR}, $\Sigma_{\rm HI}$ plotted as function of λ in parsec for three galaxies are plotted in left pannel. Red lines with star points show the correlation coefficients between $\sigma_{\rm HI}$ and $\Sigma_{\rm HI}$, black lines with square markers show that of $\sigma_{\rm HI}$ and Σ_{SFR}, blue lines with triangle markers show the same for $\sigma_{\rm HI}$ and Q_T . In right pannel, correlation coefficients between $\sigma_{\rm HI}$ and $\Sigma_{\rm H_2}$, Σ_* are plotted. Green lines with square makers show the correlation with $\Sigma_{\rm H_2}$ and the purple lines with circle show the case for Σ_*. First row shows the plots for NGC 5236, second row is for NGC 4736 and third one is for NGC 3351.

row is for NGC 4736 and the third one is for NGC 3351. Interestingly in all three galaxies, a strong correlation is visible between following pairs; $\sigma_{\rm HI} - \Sigma_{SFR}$, $\sigma_{\rm HI} - \Sigma_{\rm HI}$, $\sigma_{\rm HI} - \Sigma_*$, $\sigma_{\rm HI} - \Sigma_{\rm H_2}$ at scales greater than 1 kpc. These can be easily understood by the earlier

observation on the correlation between $\Sigma_{\rm H_2}$ and SFR at a large scale and the fact that H I disc is vertically supported by its velocity dispersion (Bigiel et al., 2008). For NGC 5236 and NGC 4736 galaxies, H I gas velocity dispersion shows a trend of anti-correlation with Q_T which keeps on increasing after 1 kpc. This means that irrespective of large scale high velocity dispersions regions in the disc, they have smaller values of Q_T. Then the gas dispersion is likely to play a role in quenching the SFR at scales smaller than we probe here. Hence the following can be inferred from this correlation trend in galaxies NGC 5236 and NGC 4736; (1) The chance of finding high H I velocity dispersion in denser gas (H I $+\rm H_2$) is regions is high, (2) Regions which are prone to instability have a high chance of finding H I gas dispersion (3) Finally high stellar mass regions and star formation regions can have high velocity dispersion. Primarily these inferences are strengthening our findings from the previous section about these two galaxies; that disc instability triggers star formation. Irrespective of the presence of high gas dispersion (or pressure), gravity is winning and can lead to cloud collapse. The positive correlation between Q_T and $\rm H_2$ gas at a large scale is also a positive sign for cloud formation through instability. In the case of NGC 3351, it shows a nearly null correlation between $\sigma_{\rm HI}$ and Q_T values. Interestingly from the findings from the previous section, we can see almost no correlation between gravitational instability and large scale star formation rate found in NGC 3351. Though H I density is positively correlated with the instability, such that high density H I gas can collapse, somehow the further process of collapsing to form GMCs and further collapse to smaller scale to form new stars is on halt or delayed. That is why even in the presence of high density $\rm H_2$, the disc seems stable in NGC 3351.

The H I column density power spectrum measurement of galaxies NGC 5236 and NGC 4736 shows the presence of turbulence cascade in the disc, with the slopes of their respective power spectra being -1.23 from 11 kpc to 300 pc and -0.7 from 7.8 kpc to 500 pc. These values of slopes essentially indicate that a significant amount of turbulence

Galaxy	$\log(M_{\rm HI})$	SFR per unit area	α	Power law range	$< \sigma_{\rm HI} >$
	$M_\odot$	$M_\odot yr^{-1}kpc^{-2}$		kpc	km s^{-1}
NGC 5236	9.3	0.07	-1.23	$0.3 - 11.0$	11.3
NGC 4736	8.6	0.042	-0.7	$0.3 - 1.0$	12.0
NGC 3351	9.1	0.009	-0.2	$0.7 - 3.0$	10.6

Table 4.3 Table shows different quantities indicating star formation and turbulence in three galaxies. Column(1) - Galaxy name, Column(2) - total H I mass, Column(3) - star formation rate per unit area, Column(4) - slope of H I column density power spectrum, Column(5) - range of length scale where power law power spectrum is measured, Column(6) - mean H I velocity dispersion.

cascade is present in these galaxies. However, the slope of the power spectrum for H I density fluctuations in NGC 3351 is quite less about -0.2 from 3 kpc to 700pc. This smaller value of the slope is almost near to a flat power spectrum which indicates the lack of presence of turbulence cascade in this disc. Surprisingly the slope of the power law of three galaxies is found to have a nice correlation with star formation rate per unit area which are as follows: NGC 5236, NGC 4736, NGC 3351 are 0.07,0.042,0.009 $M_\odot yr^{-1}kpc^{-2}$ respectively. Table 4.3 summarises the slope of the power spectrum, star formation rate per unit area, H I mean velocity dispersion and total H I mass of all three galaxies. The possible reason that gravitational instability is failing to trigger star formation in NGC 3351 is the insufficient presence of turbulence cascade in the disc.

4.5 Summary and Conclusions

In this chapter we tried to see how gravitational instability in disc galaxies is triggering star formation and how turbulence plays a significant role in this complex transformation. Successfully we probed unstable regions in disc galaxies NGC 5236, NGC 4736 and NGC 3351 and tried to see how these regions are correlated with the density of different

components in the galaxies. Based on our results and inferences, we reach the following conclusions.

- All three galaxies are found to have unstable regions in their discs, mostly populated in the spiral arms, high star forming rings etc.
- The gravitational force is the sole driving factor of disc instability at scales > 0.5 kpc. At smaller scales, other effects start to play a role.
- Among the three galaxies, NGC 3351 has been found to have an insignificant turbulence cascade present in the disc while the other two galaxies have a significant presence of turbulence. This galaxy also shows less relation with instability at the scales we probe with star formation. This implies that the presence of turbulence is an inevitable factor in star formation.
- The high density gas regions become gravitationally unstable and collapse. But it is not necessary that this gas can collapse always so that it reaches Jeans length and hence lead to the next level structure formation. But if strong enough turbulence is present, it can compress the gases to much smaller scales, so that they can reach the criteria to form new structures and hence eventually induce star formation. Our results highlight how the presence of turbulence is speeding the star formation process in NGC 5236 and NGC 4736 and how its absence delays star formation in NGC 3351.
- We do not observe the effect of velocity dispersion on quenching the star formation, indicating its effectiveness is at scales < 300 pc or lower.